Journal of Materials Science: Materials in Electronics (2020) 31:15530–15538
https://doi.org/10.1007/s10854-020-04115-x

The role of a nonconductive film (NCF) on Cu/Ni/Sn-Ag microbump interconnect reliability

Hyodong Ryu[1] · Kirak Son[1] · Jeong Sam Han[2] · Young-Bae Park[1] · Tae-Kyu Lee[3]

Received: 26 May 2020 / Accepted: 27 July 2020 / Published online: 11 August 2020
© Springer Science+Business Media, LLC, part of Springer Nature 2020

Abstract

The use of a nonconductive film (NCF) to establish and enhance the stability of microbumps is crucial. Even though it is normal to apply NCF to microbump interconnection layers, understanding the behavior of microbump stability without the protection from a NCF is important. A free standing structure without a NCF can be used to determine the mechanical response of a single microbump. This information can be used to design robust interconnect structures. Electromigration (EM) tests were performed at 150 ℃ and 1.3×10^5 A/cm^2 to investigate the effect of a NCF on the electrical reliability of Cu/Ni/Sn-Ag microbumps. The EM test results show different failure times and failure modes for Cu/Ni/Sn-Ag microbumps with the NCF and without the NCF. The microbump test samples with the NCF had a time to failure that was three times longer than that without the NCF. At a constant current density condition, the contribution of temperature-induced accelerated degradation and mechanical deformation factors were considered. A series of finite element and electron backscattered diffraction analyses revealed that the NCF restricted solder deformation and led to an increase in the back stress, which prolonged the EM lifetime.

1 Introduction

Due to the rapid development of miniature, lightweight, high-performance, and multifunctional electronic devices, electronic device packages are adopting multipin and fine pitch structures to increase performance. Three-dimensional (3D) chip stack structures integrating various functional chips have been designed and developed [1–4]. Along with flip-chip packaging technology, multistacked structures with fine and complex designs have been increasingly used in the electronics industry in recent years [3–5]. Though challenges remain, solder bumps are limited to a fine pitch below 100 µm because of the increased risk of bump bridging and misalignment. Even smaller bumps have been implemented and enabled, which increases in the current density, leading to an increased risk of electromigration (EM)-induced failure modes [6, 7]. Underfill has been commonly used in flip-chip joints and provides structural stabilization between the chip and substrate. It also relieves stress concentrations in the interconnections located at the perimeter of the chip and ensures reliable thermal cycling performance [8–16]. However, a fine pitch below 100 µm is in great demand, and two major challenges need to be overcome: the formation of voids within the underfill material and microbump bridging [17–19]. These two major risks can be mitigated with the use of nonconductive film (NCF). The application of a NCF, as an alternative to the conventional underfill process, demonstrates less voiding than a conventional underfill material, and the assembly process can be simplified [20–23]. Various studies were conducted to correlate the underfill material and EM. Yamanaka et al. reported the underfill effect on EM lifetime; it was found that the lifetime was closely correlated to the back stress because the underfill material restricted solder deformation [24]. A simulation study on different underfill materials revealed that a change in the Young's modulus of the underfill had little

✉ Young-Bae Park
ybpark@anu.ac.kr

✉ Tae-Kyu Lee
taeklee@pdx.edu

[1] School of Materials Science and Engineering, Andong National University, Andong-si, Gyeongsangbuk-do 36729, Republic of Korea

[2] Department of Mechanical & Robotics Engineering, Andong National University, Andong-si, Gyeongsangbuk-do 36729, Republic of Korea

[3] Mechanical and Materials Engineering, Portland State University, Portland, OR 97201, USA

impact on the current density and temperature distribution but impacted the bump deformation and hydrostatic stress distributions [25]. Various publications are available that consider the relationships between a NCF and humidity and the thermal cycling reliability of microbumps, but a limited number of reports are available that correlate NCF materials and interconnect EM response [26, 27]. This study considers the effect of NCF on the EM interconnect reliability of Cu/Ni/Sn-Ag microbumps. Microbump structures with and without a NCF were prepared and EM tested. 3D finite element analysis (FEA) was performed to determine the distribution of Joule heating and thermal stresses. Electron backscattered diffraction (EBSD) was performed to identify any localized strain and stress distributions and determine the baseline thermomechanical responses of the interconnects to understand the effect of the NCF.

2 Experimental procedures

The test vehicle used in this study comprised the stacked multichip components shown in Fig. 1, which consisted of a top and bottom chip with dimensions of 5 × 5 mm^2 and 10 × 10 mm^2, respectively. Both the top and bottom chips had identical thicknesses and bump structures, as each had Cu pillars with a 100 μm pitch, 20 μm diameter, and 8 μm height. A Sn-Ag solder was electroplated on a 5 μm Ni

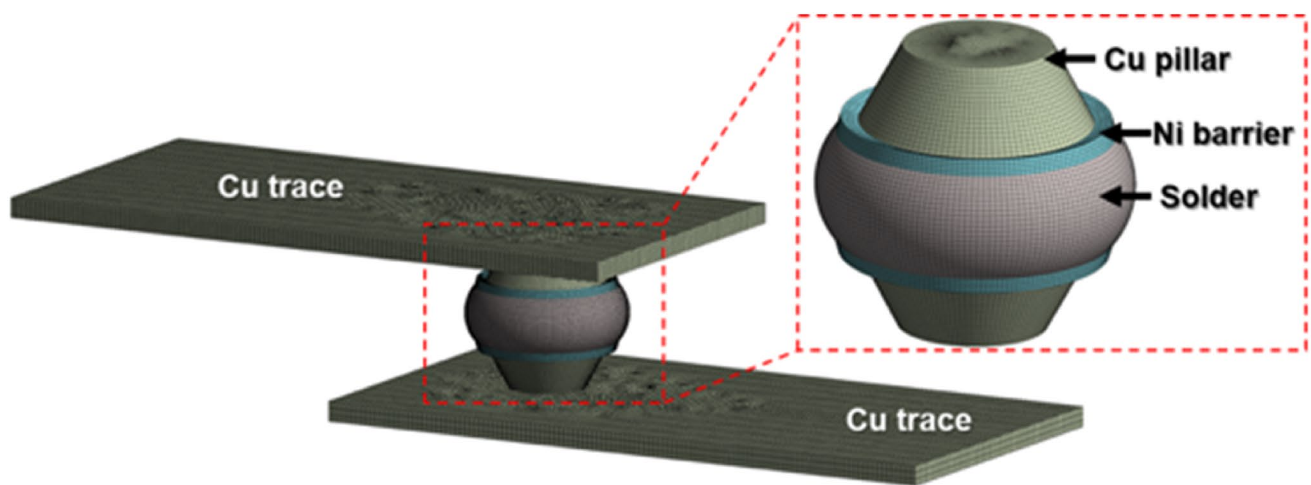

(a)

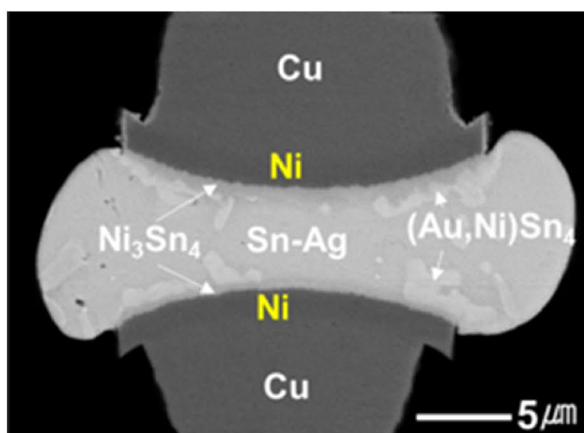

(b)

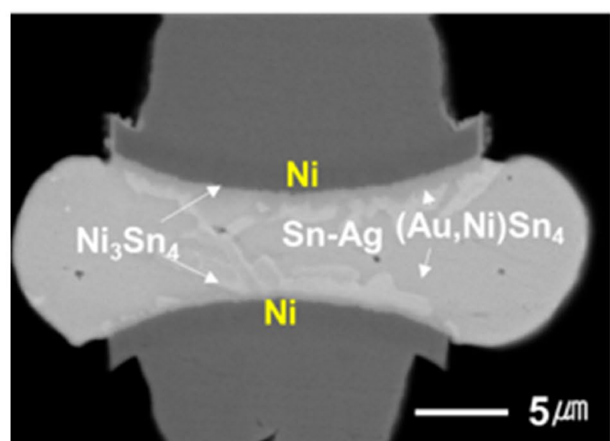

(c)

Fig. 1 **a** 3D finite element model showing the structures in the Cu/Ni/Sn-Ag microbump. Initial microstructure after thermo-compression bonding of Cu/Ni/Sn-Ag microbumps **b** with the NCF and **c** without the NCF observed with SEM

barrier for the top die before the thermo-compression bonding assembly process was done. The bottom die contained 1 µm electroplated Au on top of the Ni barrier to improve the wettability of the bonding interface during assembly [28]. Bonding was performed using a thermo-compression bonder after the NCF was dispensed over the Au/Ni/Cu pillars on the bottom chip. The peak reflow temperature and bonding load were 260 ℃ and 20 N, respectively. For the Cu/Ni/Sn-Ag microbump samples without the NCF, bonding was performed using the same thermo-compression parameters without dispensing the NCF over the Au/Ni/Cu pillars on the bottom chip. A schematic of the structure and initial cross-sectional view after thermo-compression bonding for each sample structure is shown in Fig. 1a–c. The overall heights of the microbumps after thermo-compression bonding were identical due to the same bonding parameters. For EM testing, a constant current of 0.408 A was applied to each sample condition, which resulted in an average current density of 1.3×10^5 A/cm^2 at a constant temperature of 150 ℃. The resistance change was monitored in-situ using a control unit and power supply. To investigate the microstructural changes and failure modes in the solder joints induced by the EM tests, a set of microbumps were cross-sectioned before and after current stressing at various periods of time and examined with scanning electron microscopy (SEM) and EBSD. FEA analyses using ANSYS 18.2 were performed to determine the distribution of Joule heating and thermal stresses within the stacked multichip package under the current stressed conditions. The finite element model used in this study consisted of the SOLID226 3D 20-node thermo-electric coupled-field solid element provided by ANSYS. The temperature distributions used in the thermal stress analysis were imported from the results of the Joule heating simulation. Furthermore, the stress-free temperature was set to 298 K. The material properties used in the Joule heating and thermal stress analyses are listed in Tables 1 and 2, respectively.

3 Results and discussion

Figure 2 shows the electrical resistance changes of the Cu/Ni/Sn-Ag microbumps with and without the NCF. For the Cu/Ni/Sn-Ag microbump without the NCF, the time to failure was approximately 196 h, while it was approximately 572 h with the NCF under a current density of 1.3×10^5 A/cm^2 and at a temperature of 150 ℃. For both cases, the resistance increased linearly and then abruptly increased afterward. Compared to the NCF applied sample, the sample without NCF microbumps showed higher acceleration in resistance increase from the beginning and a much faster increase than the sample with NCF applied microbumps. In both sample configurations, the constant increase in the resistance was possibly due to the consumption of the Ni barrier and the formation of a Ni–Sn intermetallic compound (IMC), and the subsequent rapid increase in the resistance was due to the exhaustion of the Ni barrier and accelerated formation of Cu-Sn IMCs. Thus, the possible reason for the

Table 1 Material properties of the Joule heating simulation

Materials	Thermal conductivity (W/m·K)	Resistivity (mΩ·cm)	Temperature coefficient of resistivity (K^{-1})	Source
Sn-2.5Ag	33	12.3	4.6×10^{-3}	[25]
Ni	76	28	6.8×10^{-3}	[31]
Cu	403	6.8	4.3×10^{-3}	[25]
Wafer-level NCF	0.55	–	–	[25]
Si	147	–	–	[32]

Table 2 Material properties of thermal stress simulation

Materials	Model	E (GPa)	CTE(ppm/K)	Poison ratio	Source
Sn-2.5Ag	Temperature-dependent elastic-isotropic	46.8 @ 298 K 26 @ 433 K	22.5	0.4	[33]
Ni	Elastic-isotropic	186	12.5	0.342	[34]
Cu	Elastic-isotropic	122	17.1	0.35	[35]
Wafer-level NCF	Temperature-dependent elastic-isotropic	6.4 @ 223 K 6 @ 273 K 5.6 @ 298 K 4.5 @ 353 K 2.3 @ 398 K	45		[35]
Si	Elastic-isotropic	169.5	3	0.28	[35]

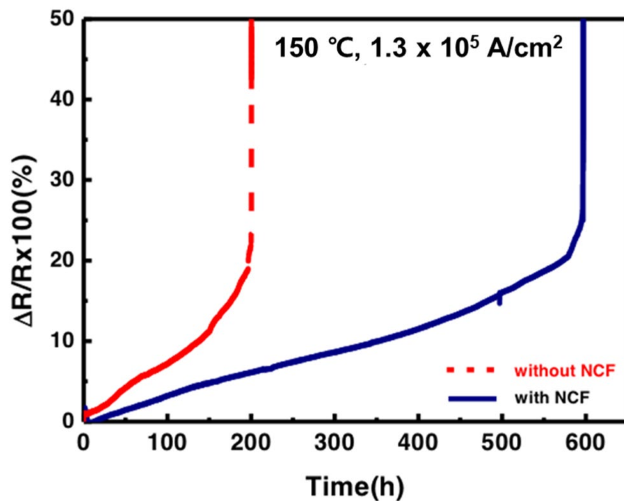

Fig. 2 Relative changes in the electrical resistance with increasing current stressing time of Cu/Ni/Sn-Ag microbumps with and without the NCF at 150 ℃ with a current density of 1.3×10^5 A/cm^2

main difference in the resistance increase between the samples with and without the NCF, shown in Fig. 2, seems to have been caused by the difference in the growth rate of the IMCs. Based on the resistance change curve alone, the NCF prolonged the EM time to failure by 291% for the Cu/Ni/Sn-Ag microbumps compared to that for the sample without the NCF. The cross-sectioned Cu/Ni/Sn-Ag microbumps with the NCF before and after the current stressing for 600 h at 150 ℃ with a current density of 1.3×10^5 A/cm^2 are shown in Fig. 3a and b. Prior to the current stressing, as shown in Fig. 1b and c, $(Au,Ni)Sn_4$ and Ni_3Sn_4 IMCs were observed in the bulk Sn-Ag solder. Following current stressing, the failure of Cu/Ni/Sn-Ag microbumps without the NCF was related to the consumption of the Cu pillar and Ni barrier, as shown in Fig. 3a and b, respectively. The arrow marks the direction of electron flow. In the bump with the downward flow of electrons, as shown in Fig. 3a, the Ni barrier edge on the cathode into which the electrons flow was consumed by the reaction with Sn. As a result, the Sn and Cu pillars beneath the Ni barrier at the bottom chip were transformed into $(Cu,Ni)_6Sn_5$ and Cu_3Sn IMCs. In addition, the dissolution of nearly the entire Ni barrier on the cathode side was observed after 600 h of EM testing. A large amount of $(Cu,Ni)_6Sn_5$ IMC was observed in the middle of the solder bump. In the opposite case for the downward electron flow, as shown in Fig. 3b, the symmetrical structure at the top and bottom resulted in the formation of IMCs, similar to the case with the upward electron flow. Figure 3c and d show SEM images of the cross-sectioned Cu/Ni/Sn-Ag microbumps without the NCF after current stressing for 200 h at 150 ℃ with a current density of 1.3×10^5 A/cm^2. The Ni barrier on the cathode was fully consumed by the formation of $(Cu,Ni)_6Sn_5$ IMC, regardless of the electron flow. Although the time to failure was significantly different, the EM-induced degradation at the interconnect was similar for the Cu/Ni/Sn-Ag microbumps with and without the NCF, regardless of the prolonged current stressing time. Similar observations were made on the underfill effects of solder bumps reported in previous studies, where the back stress was increased by the confinement of the underfill, and it was relieved by solder deformation, resulting in an increased EM time to failure [24]. A comparison of the microbumps with and without the NCF indicated that a height difference after EM testing can be seen. The microbumps with the NCF maintained a constant bump height after the EM test for 600 h compared to the initial bump height shown in Fig. 1b. However, the microbumps without the NCF revealed an increase in bump heights after EM for both the upward and downward current stressed bumps after 200 h, as shown in Fig. 3c and d. Given that the initial bump heights were identical initially, a height increase was expected to occur during EM. The microbumps without the NCF were expected to have fewer constraints and be able to maintain the gap distance between the stacked dies, resulting in a net positive increase in the bump height. Additionally, plastic deformation during EM increased the defect density and accelerated the diffusion of the microbumps, resulting in an accelerated IMC growth rate, which explains the accelerated increase in the resistance in Fig. 2.

In general, the mass transport by EM in a pure metal material in a strip structure can be expressed by the following equation [29, 30]:

$$J = \frac{CD}{KT}\left(Z^{*}e\rho j - \Omega\frac{d\sigma}{dx}\right) \tag{1}$$

where J is the net atomic flux from EM, and $C, D, k, T, Z^{*}, e, \rho, j, \Omega$, and $d\sigma/dx$ are the atomic concentration, the diffusivity, Boltzmann's constant, the absolute temperature, the effective charge number, the electron charge, the resistivity, the current density, the atomic volume, and the back stress gradient (σ is the hydrostatic stress in the material), respectively. The first term on the right-hand side of the equation represents the atomic flux due to the EM drift force, while the second term represents the backflow due to the back stress. Thus, there is no net EM drift when these two forces are balanced, and the critical length is defined as a length in this condition. Based on the backflow concept, the effect of the NCF on the EM failure time indicated that the NCF increased the back stress and inhibited net atomic movement since the other variables on the right-hand side of Eq. (1) were the same [24].

To identify the NCF effect on Joule heating and thermal stresses, FEA simulations were performed. Figure 4 shows the current density distribution under a current of 0.408 A at a temperature of 150℃. Figure 4a and b show the

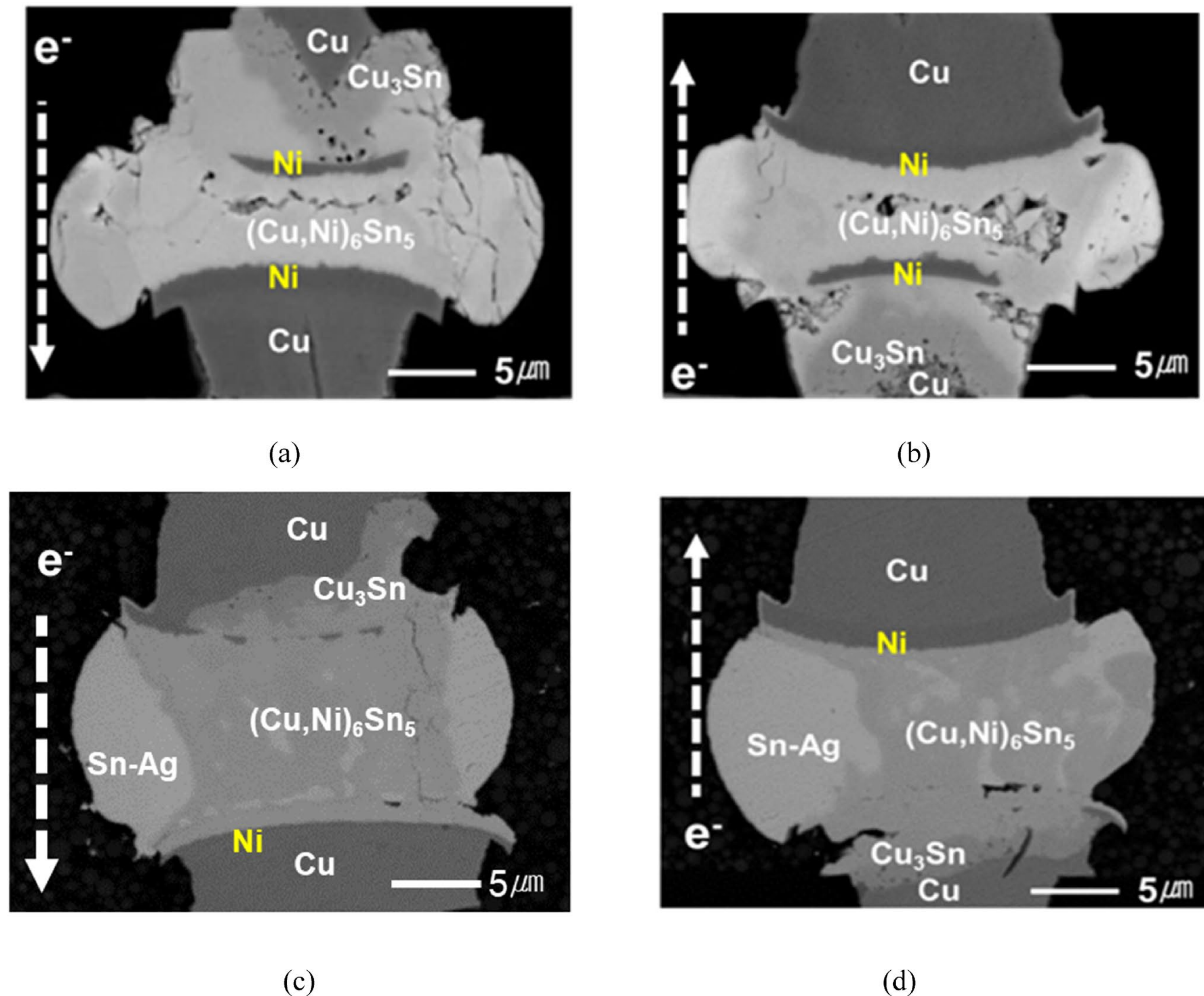

Fig. 3 SEM images of the cross-sectioned surface of Cu/Ni/Sn-Ag microbumps (**a**) (**b**) with the NCF after current stressing for 600 h and (**c**) (**d**) without the NCF for 200 h at 1.3×10^5 A/cm^2 and 150 ℃. **a c** Images after downward current stressing and **b d** upward current stressing

current density distributions in the Cu/Ni/Sn-Ag microbumps with and without the NCF during the EM test. The maximum current density for the microbump with the NCF in Fig. 4a and b is 1.77×10^6 A/cm^2, which occurred near the interface between the Cu trace and Cu pillar. Due to the small diameter of the microbumps, the difference in the cross-sectional area between the traces and the microbumps was not large. Therefore, the maximum current density inside the solder region was only 1.57×10^5 A/cm^2, with an average density of 1.3×10^5 A/cm^2. The temperature distribution in Fig. 4c indicated that the maximum temperature of the hot spot was 161.2 ℃ at the bottom chip area. In comparison, the simulation results for the Cu/Ni/Sn-Ag microbumps without the NCF indicated that the maximum temperature of 163.2 ℃ was also at the bottom chip area, as shown in Fig. 4d.

In terms of the temperature distribution, for the Cu/Ni/Sn-Ag microbumps without the NCF, the maximum temperature was approximately 2 ℃ higher than that of the Cu/Ni/Sn-Ag microbumps with the NCF. This increase contributed to the higher acceleration of the IMC formation in the microbumps without the NCF, but the temperature difference was expected to have a minimal effect. There was a minimal differentiation in the maximum temperature between the microbumps with and without the NCF. Figure 5 represents the distribution of hydrostatic stresses in the Sn-Ag solder of the Cu/Ni/Sn-Ag microbumps under a current of 0.408 A at 150 ℃ to confirm the effect of the back stress on the NCF application. Figure 5a shows the hydrostatic stress distribution in the Cu/Ni/Sn-Ag microbumps with the NCF during the EM test. The edge of the solder had a compressive stress of 34.6 MPa, since both the NCF and solder expanded due

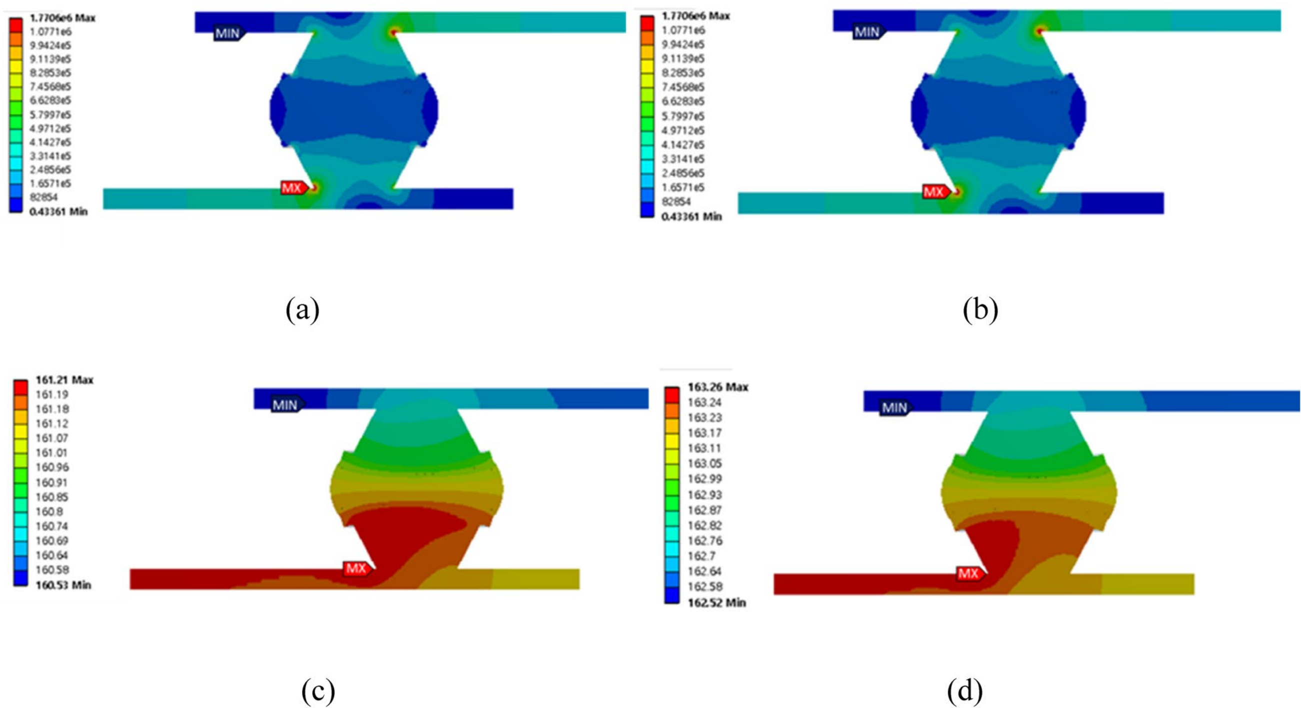

Fig. 4 FEM simulation results for the current density distribution **a b** and temperature distribution **c d** in microbumps with and without the NCF microbump under a current of 0.408 A at 150 ℃

to the increased temperature. The top and bottom centers of the solder had a tensile stress of 199 MPa due to the expansion of the NCF in the vertical direction. Because of the dissimilar coefficients of thermal expansion (CTE) between the NCF and the solder material, the solder bumps were also strained in the vertical direction. Figure 5b shows the hydrostatic stress distribution in the Cu/Ni/Sn-Ag microbumps without the NCF during the EM test. Because the under-bump metallization structure had a lower CTE value than the solder, the center of the solder had a compressive stress of 30 MPa induced by its inhibited expansion. On the other hand, the edge of the solder showed a tensile stress of 19 MPa since the side of the solder expanded freely with increasing temperature. According to the FEA results, the NCF application had little impact on the current density distribution and a minimal effect on the temperature distribution. However, the strain inhibition at the edges of the bump and vertical deformation increased the overall hydrostatic stress distribution in the solder, which contributed to an increase in the back stress during EM. Even though the impact was minimal, the higher stress level in the center of the microbumps with the NCF created a condition that can limit diffusion compared to lower stress level in the microbumps without the NCF.

The EBSD analysis of the microbumps before and after the EM testing is comparable to the FEA analysis and observations. The EBSD images of the initial state of the microbumps with the NCF before current stressing (Fig. 6a) and after current stressing (Fig. 6b). The energy-dispersive X-ray spectroscopy (EDS) map of the Ag distribution revealed that the once uniformly distributed Ag_3Sn intermetallic precipitates shifted to the top region near the IMC interface that was aligned with the upward current direction. The band contrast image and inverse pole figure (IPF) images indicated that the number of small Sn grains increased after current stressing for 600 h with an overall decrease in the localized strain, which can be seen with the strain contour map. However, as indicated by the white box in the strain contour map and grain reference orientation distribution (GROD) map, a higher level of strain and residual stress is observed for the microbumps with the NCF. Figure 6c and d show the microbump without the NCF. The tendency of the grains to grow after current stressing is similar to that for the microbumps with the NCF, and Ag_3Sn intermetallic precipitates also accumulated and shifted and became aligned to the downward current direction. However, unlike the microbumps with the NCF after EM, the microbumps without the NCF had a more decentralized local strain and residual stress distribution, as indicated by the white boxes. The series of EBSD observations is consistent with the FEA analysis, which indicates a centralized stress for microbumps with the NCF and a decentralized stress distribution for microbumps without the NCF.

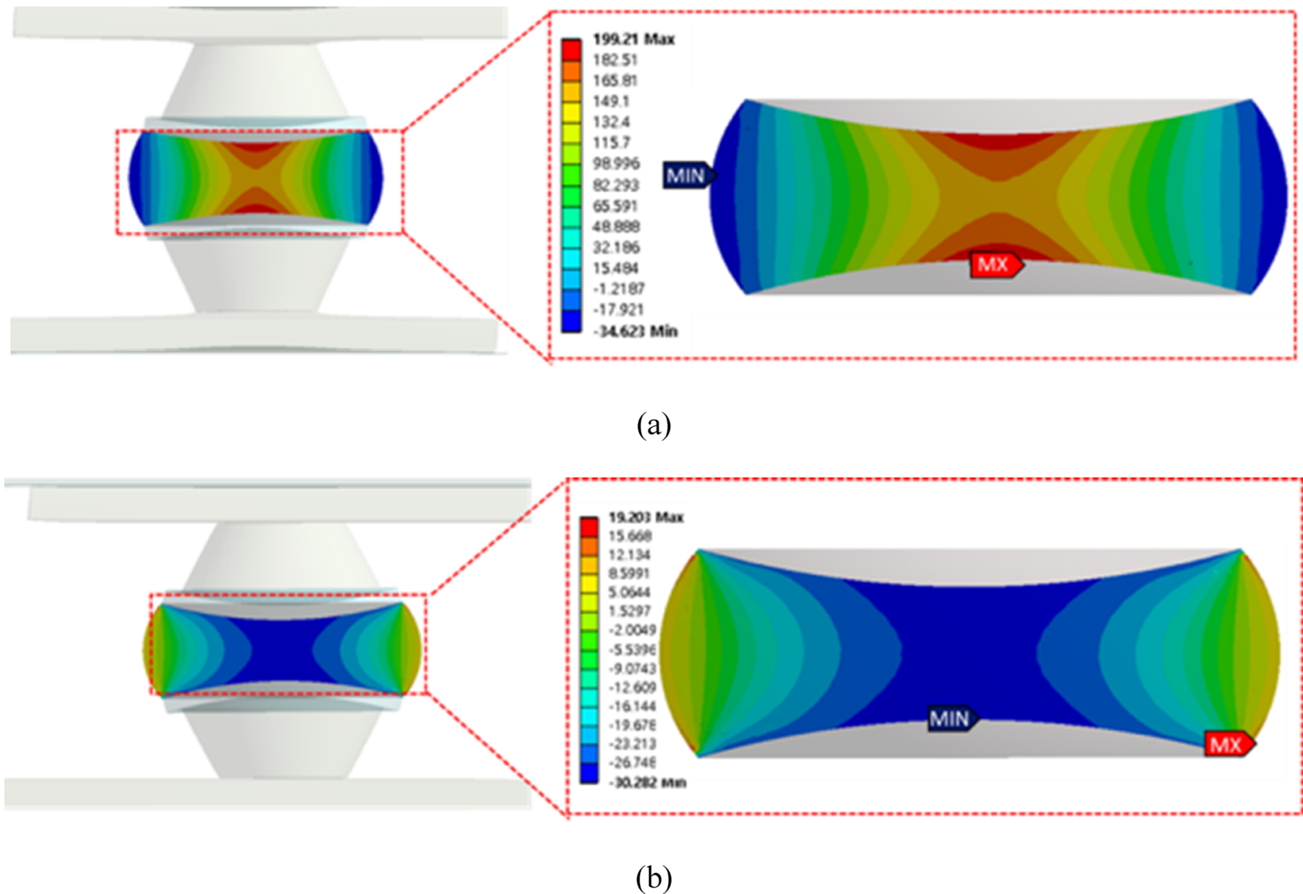

Fig. 5 FEA simulation results for the hydrostatic stress distribution in **a** with the NCF microbump and **b** without the NCF microbump under a current of 0.408 A at 150 ℃

4 Conclusion

EM phenomena were investigated in Cu/Ni/Sn-Ag microbumps. Two types of microbumps were fabricated with the same solder material according to the presence of NCF: one was encapsulated with the NCF, while the other was not encapsulated with NCF. The EM tests were performed under a current density of 1.3×10^5 A/cm^2 and at 150 ℃. The presence of the NCF improved the EM failure time of the Cu/Ni/Sn-Ag microbumps. The FEA revealed that the application of the NCF limited the solder deformation and increased the total hydrostatic stress inside the solder. Based on these results, the strain inhibition of the solder sides and vertical deformation increased the overall hydrostatic stress in the solder, which is considered to indirectly contribute to an increase in the back stress during EM. Additionally, as a result of EBSD analysis, a higher level of strain and residual stress is observed for the microbumps with the NCF compared to the microbumps without the NCF. Thus, it was concluded that the increase in the back stress due to the restriction of solder deformation by NCF increased the EM lifetime.

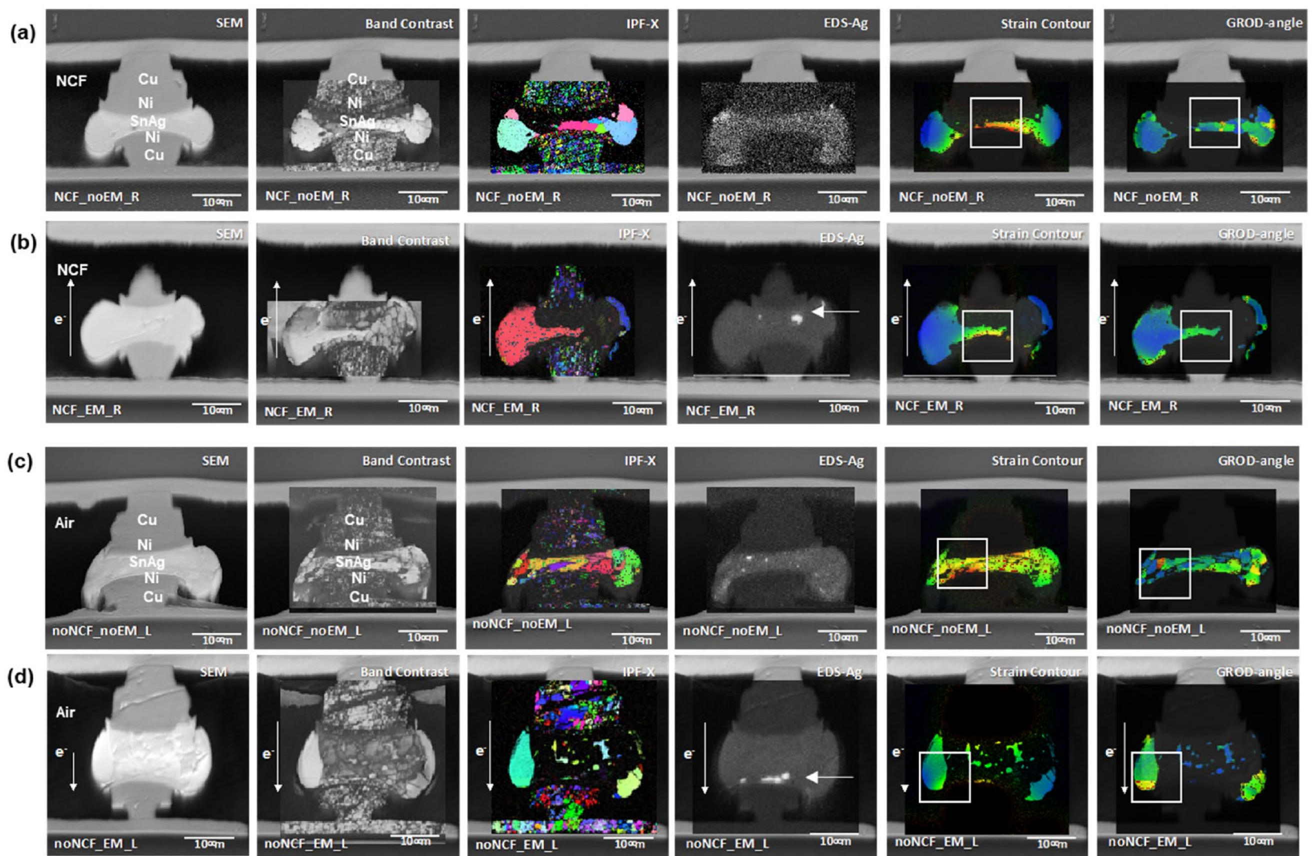

Fig. 6 SEM and EBSD images of Cu/Ni/Sn-Ag microbumps **a** before and **b** after current stressing for 600 h with the NCF and **c** before and **d** after 200 h EM without the NCF at 1.3×10^5 A/cm^2 and 150 ℃

Acknowledgements This research was supported by Basic Science Research Program through the National Research Foundation of Korea (NRF) funded by the Ministry of Education (2019R1D1A3A03103823), and also by MOTIE(Ministry of Trade, Industry & Energy (20003524) and KSRC(Korea Semiconductor Research Consortium) support program for the development of the future semiconductor device. The authors would like to thank Dr. H.Y. Son and N.S. Kim from SK Hynix Inc. for valuable discussions and test sample preparations.

References

1. J.R. Lloyd, J. Phys. D: Appl. Phys. **32**, 109 (1999)
2. K.N. Tu, K. Zeng, Mater. Sci. Eng. **34**, 1 (2001)
3. T.S. Oh, K.Y. Lee, Y.H. Lee, B.Y. Jung, Met. Mater. Int. **15**, 479 (2009)
4. J. Cho, E. Yoon, Y. Park, W.J. Ha, J.K. Kim, Electron. Mater. Lett. **6**, 51 (2010)
5. R.R. Tummala, *Fundamentals of microsystems packaging* (McGraw-Hill, New York, 2001)
6. J.H. Lee, G.T. Lim, S.T. Yang, M.S. Suh, Q.H. Chung, K.Y. Byun, Y.B. Park, J. Kor. Inst. Met. & Mater. **46**, 310 (2008)
7. G.T. Park, B.R. Lee, K. Son, Y.B. Park, Electron. Mater. Lett. **15**, 149 (2019)
8. W.J. Choi, E.C.C. Yeh, K.N. Tu, J. Appl. Phys. **94**, 5665 (2003)
9. K.M. Chen, J.D. Wu, K.N. Chiang, Microelectron. Reliab. **46**, 2104 (2006)
10. K.N. Chiang, C.C. Lee, C.C. Lee, K.M. Chen, Appl. Phys. Lett. **88**, 072102 (2006)
11. H.Y. Basaran, D.C. Hopkins, Int. J. Damage Mech. **15**, 41 (2006)
12. J. H. Lee, Y. D. Lee, Y. B. Park, S. T. Yang, M. S. Suh, Q. H. Chung, and K. Y. Byun, Proceedings of 57th Electronic Components and Technology Conference (2007)
13. K. Yamanaka, Y. Tsukada, K. Suganuma, Microelectron. Reliab. **47**, 1280 (2007)
14. K. Yamanaka, Y. Tsukada, K. Suganuma, J. Alloys Compd. **437**, 186 (2007)
15. Y.S. Lai, K.M. Chen, C.L. Kao, C.W. Lee, Y.T. Chiu, Microelectron. Reliab. **47**, 1273 (2007)
16. D. Yang, Y.C. Chan, K.N. Tu, Appl. Phys. Lett. **93**, 041907 (2008)
17. M.K. Schwiebert, W.H. Leong, IEEE, T. Electron. Pa. M. **19**, 133 (1996)
18. H. Peng, R.W. Johnson, IEEE, T. Electron. Pa. M. **4**, 293 (2001)
19. S.T. Lu, Y.M. Lin, C.C. Chuang, T.H. Chen, W.H. Chen, IEEE Trans. Compon. Packag. Manuf. Technol. **1**, 33 (2011)
20. C. Feger, N. Labianca, M. Gaynes, S. Steen, Z. Liu, and R. Peddi, Proceedings of 59th Electronic Components and Technology Conference (2009)
21. K. Honda, T. Enomoto, A. Nagai, and N. Takano, Proceedings of 60th Electronic Components and Technology Conference (ECTC) (2010)

22. T. F. Yang, K. S. Kao, R. S. Cheng, J. Y. Chang, and C. J. Zhan, Proceedings of 2011 IEEE International Conference on Electronics Packaging (ICEP) (2011)
23. S. Kawamoto, M. Yoshida, S. Teraki, and H. Iida, Proceedings of 62nd Electronic Components and Technology Conference (2012)
24. K. Yamanaka, T. Ooyoshi, T. Nejime, J. Alloy. Compd. **481**, 659 (2009)
25. S. R. Rao, Proceedings of 63rd Electronic Components and Technology Conference (2013)
26. S.C. Kim, Y.H. Kim, J Mater Sci: Mater Electron. **27**, 3658 (2015)
27. B.I. Noh, J.W. Yoon, S.B. Jung, I.E.E.E.T. Comp, Pack. Man. **32**, 633 (2009)
28. J. Glazer, P.A. Kramer, J.W. Morris, Circuit World **18**, 41 (1992)
29. I.A. Blech, J. Appl. Phys. **47**, 1203 (1976)
30. I.A. Blech, Acta Mater. **46**, 3717 (1998)
31. W.C. Kuan, S.W. Liang, C. Chen, Microelectron. Reliab. **49**, 544 (2009)
32. L. Meinshausen, K. Weide-Zaage, and M. Petzold, Proceedings of 61st Electronic Components and Technology Conference (2011)
33. F. M. Tzu, L. S. Chao, and J. H. Chou, Proceedings of International Microsystems, Packaging, Assembly and Circuits Technology (2007)
34. C. Liu, S. M. Chen, F. W. Kuo, H. N. Chen, E. H. Yeh, Proceedings of International Electron Devices Meeting (2012)
35. A. Yeo, C. Lee, J.H.L. Pang, I.E.E.E.T. Comp, Pack. Man. **29**, 355 (2006)

Publisher's Note Springer Nature remains neutral with regard to jurisdictional claims in published maps and institutional affiliations.